NASA TECHNICAL NOTE

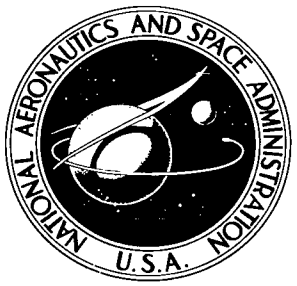

NASA TN D-6582

NUMERICAL CALCULATION OF TRANSONIC FLOW ABOUT SLENDER BODIES OF REVOLUTION

by Frank R. Bailey

Ames Research Center
Moffett Field, Calif. 94035

NATIONAL AERONAUTICS AND SPACE ADMINISTRATION • WASHINGTON, D. C. • DECEMBER 1971

1. Report No.	2. Government Accession No.	3. Recipient's Catalog No.
NASA TN D-6582		

4. Title and Subtitle	5. Report Date
NUMERICAL CALCULATION OF TRANSONIC FLOW ABOUT SLENDER BODIES OF REVOLUTION	December 1971
	6. Performing Organization Code
7. Author(s)	8. Performing Organization Report No.
Frank R. Bailey	A-4115
	10. Work Unit No.
9. Performing Organization Name and Address	126-13-10-19-00-21
Ames Research Center, NASA Moffett Field, Calif., 94035	11. Contract or Grant No.
	13. Type of Report and Period Covered
12. Sponsoring Agency Name and Address	Technical Note
National Aeronautics and Space Administration Washington, D. C., 20546	14. Sponsoring Agency Code

15. Supplementary Notes

16. Abstract

This paper describes a relaxation method for the numerical solution of the transonic small disturbance equation for flow about a slender body of revolution. Results for parabolic arc bodies, both with and without an attached sting, are compared with wind-tunnel measurements for a free-stream Mach number range from 0.90 to 1.20. The method is also used to show the effects of wind-tunnel wall interference by including boundary conditions representing porous-wall and open-jet wind-tunnel test sections.

17. Key Words (Suggested by Author(s))	18. Distribution Statement
Transonic flow Slender bodies Axisymmetric bodies	Unclassified – Unlimited

19. Security Classif. (of this report)	20. Security Classif. (of this page)	21. No. of Pages	22. Price*
Unclassified	Unclassified	39	$3.00

*For sale by the National Technical Information Service, Springfield, Virginia 22151

SYMBOLS

A_k, B_k, C_k	discrete radial derivative coefficients
a,b	radial transformation parameters
C_D	surface pressure drag coefficient $\int_0^1 C_p \frac{dS}{dx}\, dx$
C_p	pressure coefficient $\frac{p-p_\infty}{(1/2)\rho_\infty U_\infty{}^2}$
$C_p{}^*$	critical pressure coefficient
d	body diameter
$F_{j,k}$	defined by equations (22) and (23)
f	fineness ratio, $\frac{l}{d}$
H	defined in equation (19a)
l	body length
M_∞	free-stream Mach number
P	porosity parameter
R	body radius
S	body cross-sectional area
U_∞	free-stream velocity
u,v	perturbation velocities
x,r	cylindrical coordinates (see fig. 1)
β	$\sqrt{\lvert 1 - M_\infty{}^2 \rvert}$
γ	radio of specific heats
Δr	radial step size
Δx	streamwise step size
$\Delta\eta$	stretched radial step size

η	stretched radial coordinate
λ	$\beta^2 - M_\infty^2 (\gamma + 1) \phi_x$
ϕ	perturbation potential

Subscripts

j,k	grid index
x,r	differentiation

NUMERICAL CALCULATION OF TRANSONIC FLOW ABOUT SLENDER BODIES OF REVOLUTION

Frank R. Bailey

Ames Research Center

SUMMARY

This paper describes a relaxation method for the numerical solution of the transonic small disturbance equation for flow about a slender body of revolution. Results for parabolic arc bodies, both with and without an attached sting, are compared with wind-tunnel measurements for a free-stream Mach number range from 0.90 to 1.20. The method is also used to show the effects of wind-tunnel wall interference by including boundary conditions representing porous-wall and open-jet wind-tunnel test sections.

INTRODUCTION

There is currently a renewed interest in the study of transonic aerodynamics as it applies to a variety of practical problems such as the design of minimum-drag, transonic cruise configurations for transport aircraft. Because of the complexity and dominant nonlinearity of mixed transonic flows, the development of calculative techniques for predicting transonic aerodynamic characteristics has lagged behind the development of techniques for subsonic and supersonic flows. Very recently, however, numerical methods have been developed to predict inviscid flows, including embedded shocks, about two-dimensional airfoils at high subsonic Mach numbers. The most efficient techniques at present (refs. 1–3) use relaxation methods to solve finite-difference approximations to the governing isentropic steady-state equations. The present work uses a relaxation method to calculate steady, inviscid, transonic flow about pointed slender bodies of revolution at zero yaw. The numerical method, based on the transonic small disturbance equation, extends relaxation methods to the entire transonic regime, including both subsonic and supersonic free-stream Mach numbers. Boundary conditions in the outer flow are used to simulate a body in free air, in an open jet, and in a wind tunnel having an ideal porous wall.

BASIC EQUATIONS AND BOUNDARY CONDITIONS

Consider the inviscid, compressible flow about a slender, pointed body of revolution in cylindrical coordinates x and r (made dimensionless with respect to the length of the body) with the x-axis parallel to the free-stream velocity U_∞ (see fig. 1). Assume that all shock waves are weak enough to make vorticity negligible. Under this assumption a velocity potential can be used to calculate the flow field. In particular, a perturbation potential can be defined such that the

perturbation velocities, made dimensionless with respect to the free-stream velocity, are $u = \phi_x$ parallel to the x-axis, and $v = \phi_r$ parallel to the r-axis.

The governing differential equation for transonic flow given by slender body theory (see, e.g., ref. 4, ch. 2) can be written as

$$\lambda\phi_{xx} + \frac{1}{r}(r\phi_r)_r = 0 \tag{1a}$$

where

$$\lambda = \beta^2 - M_\infty{}^2(\gamma + 1)\phi_x$$

$$\beta^2 = 1 - M_\infty{}^2$$

M_∞ is the free-stream Mach number, and γ is the ratio of specific heats ($\gamma = 1.4$ for air). Note that the term

$$M_\infty{}^2(\gamma + 1)\phi_x$$

in the expression for λ makes the transonic equation both nonlinear and of mixed elliptic-hyperbolic type. If λ is positive, equation (1) is elliptic and represents locally subsonic flow; if λ is negative, equation (1) is hyperbolic and represents locally supersonic flow. The mixed character of the flow field may occur with local supersonic regions embedded in a subsonic flow or with local subsonic regions embedded in a supersonic flow. It should be noted that equation (1) is also valid in purely subsonic and supersonic flows up to a free-stream Mach number of approximately 2 or 3 if the body is sufficiently slender.

To complete the specification of the problem boundary conditions must be given at the body and in the outer flow. The flow tangency condition at the body surface given by the first-order slender-body approximation is that near the body axis

$$\lim_{r \to 0} (r\phi_r) = R\frac{dR}{dx} \tag{2}$$

For a body in free air the perturbation velocities vanish at infinity which is satisfied by setting ϕ equal to a constant, say zero, at infinity. In addition to the free-air boundary condition, wall boundary conditions may be given to approximate inviscid flow in open-jet and porous-wall wind-tunnel test sections. These boundary conditions can be used to illustrate wall-induced interference effects. Although the formulation is strictly valid for a circular test section, the results may be compared to a square test section of equal cross-sectional area because the effects of wall interference at the center of the tunnel should be relatively insensitive to the actual wall shape.

For an open jet, the pressure coefficient vanishes at the jet boundary, although this boundary is not parallel to the free stream when a disturbance is present. However, in the present investigation this departure is assumed small so that a vanishing pressure coefficient is imposed at a surface parallel to the free stream and coinciding with the jet boundary far upstream of the body (ref. 5). The open-jet boundary condition becomes

$$\phi_x = 0 \tag{3}$$

at the jet boundary.

The average boundary condition for a porous wall, as derived in reference 6, follows from Darcy's law for slow viscous flow through a porous medium. It is assumed that the average velocity normal to the wall is proportional to the pressure difference across the wall, which is a linearized approximation of Darcy's law for a thin wall, and that the pressure outside the wall is equal to the free-stream pressure. With the wall parallel to the x-axis, the porous wall boundary condition becomes

$$\phi_r + P\phi_x = 0 \tag{4}$$

The quantity P is a porosity parameter (or a Reynolds number of the porous medium) defined by

$$P = \frac{U_\infty \rho_\infty k}{\mu t} \tag{5}$$

where

U_∞ free-stream velocity

ρ_∞ free-stream density

k permeability of porous medium

μ viscosity of air

t tunnel-wall thickness

The permeability, k, is determined by the structure of the medium and must be found experimentally.

As the porosity parameter vanishes, equation (4) gives the boundary condition for a solid wall, and as the porosity parameter becomes large, equation (4) approaches the open jet boundary condition. It should be noted that although truly porous walls are seldom used for transonic wind tunnels, the porous wall approximation is a useful mean boundary condition for perforated walls. The actual boundary conditions for perforated walls (i.e., the combination of an open jet and solid wall) lead to a three-dimensional problem beyond the scope of the present investigation.

Finally, the slender-body approximation for the pressure coefficient at points near the body is given by

$$C_p = -2\phi_x - \phi_r^2 \tag{6}$$

and on the body surface by

$$C_p = -2\phi_x - \left(\frac{dR}{dx}\right)^2 \tag{7}$$

In transonic and supersonic flows it is necessary to take into account the discontinuous change in velocities that occur at shock surfaces. Equation (1a) written in divergence form

$$\left[\beta^2\phi_x - \frac{M_\infty^2(\gamma+1)}{2}\phi_x^2\right]_x + \frac{1}{r}(r\phi_r)_r = 0 \tag{1b}$$

can be used to show that the jump condition (see ref. 7) contained in equation (1) is given by

$$\left[\beta^2 - M_\infty^2(\gamma+1)\left(\frac{u_1+u_2}{2}\right)\right](u_1-u_2)^2 + (v_1-v_2) = 0 \tag{8}$$

$$\phi_1 = \phi_2 \tag{9}$$

where the subscript 1 refers to conditions before the jump and subscript 2 to conditions behind the jump. The corresponding Mach number and pressure jump across a normal shock for typical transonic Mach numbers can be compared with the Rankine-Hugoniot jumps, and the irrotational approximation may be considered a good one if M_1 normal to the shock surface does not exceed 1.25.

NUMERICAL METHOD

The computational domain for the numerical calculations is defined by the grid network shown in figure 2. Finite-difference approximations to the derivatives in equation (1) are constructed for each interior grid point, forming a set of nonlinear algebraic equations that are solved by relaxation techniques. In the present study both successive overrelaxation (SOR) and successive line overrelaxation (SLOR) (e.g., see ref. 8) were used. The studies showed SLOR to be superior to SOR by a factor of about 3 in computing time at subcritical Mach numbers and by as much as a factor of 10 at $M_\infty = 0.99$. Therefore, SLOR has been used to compute the results.

Of fundamental importance in using relaxation procedures in transonic flow is the concept of "mixed differencing," in which the finite difference formulas for the x-derivatives in equation (1) are locally modified to account for the mixed subsonic-supersonic character of the flow field. This modification is accomplished by testing the local value of ϕ_x to determine the sign of the term λ in equation (1). If λ is positive, indicating subsonic flow, central differences are used to account for

the domain of dependence of elliptic equations. If λ is negative, indicating supersonic flow, backward differences are used to account for the absence of upstream influence in hyperbolic equations. As a consequence of this mixed differencing, both shock waves and sonic lines evolve naturally in the course of the computation. The method is also capable of computing purely subsonic and purely supersonic flows, where λ does not change sign.

Difference Formulas

The finite difference formulation in the present method depends on the structure of the finite-difference grid and is different for subsonic and supersonic free-stream Mach numbers. In the case of a subsonic free stream the x-grid is divided into three regions (fig. 2). In the middle region, which includes the body, the x-grid is equally spaced and the x-derivatives are approximated by second-order accurate formulas. When λ is positive, the flow is locally subsonic and the formula used is

$$\lambda\phi_{XX} = \left[\beta^2 - M_\infty{}^2(\gamma + 1)\left(\frac{\phi_{j+1,k} - \phi_{j-1,k}}{2\Delta x}\right)\right]\left[\frac{\phi_{j-1,k} - 2\phi_{j,k} + \phi_{j+1,k}}{(\Delta x)^2}\right] \tag{10}$$

When λ is negative, the flow is locally supersonic and the formula (given in ref. 1) used is

$$\lambda\phi_{XX} = \left[\beta^2 - M_\infty{}^2(\gamma + 1)\left(\frac{2\phi_{j,k} - \phi_{j-1,k} - 2\phi_{j-2,k} + \phi_{j-3,k}}{2\Delta x}\right)\right]\left[\frac{2\phi_{j,k} - 5\phi_{j-1,k} + 4\phi_{j-2,k} - \phi_{j-3,k}}{(\Delta x)^2}\right] \tag{11}$$

In the regions upstream and downstream of the body an unevenly spaced x-grid is constructed with Δx progressively increasing as the upstream and downstream boundaries are approached. For locally subsonic flow a first-order accurate central difference formula is used and is given by

$$\lambda\phi_{XX} = \left[\beta^2 - M_\infty{}^2(\gamma + 1)\left(A1\phi_{j+1,k} + A2\phi_{j,k} + A3\phi_{j-1,k}\right)\right]\left[B1\phi_{j+1,k} + B2\phi_{j,k} + B3\phi_{j-1,k}\right] \tag{12}$$

where

$$A1 = \frac{\Delta x_1}{\Delta x_2(\Delta x_1 + \Delta x_2)}$$

$$A2 = \frac{\Delta x_2 - \Delta x_1}{\Delta x_1 \Delta x_2}$$

$$A3 = \frac{-\Delta x_2}{\Delta x_1(\Delta x_1 + \Delta x_2)}$$

$$B1 = \frac{2}{\Delta x_2(\Delta x_1 + \Delta x_2)}$$

$$B2 = \frac{-2}{\Delta x_1 \Delta x_2}$$

$$B3 = \frac{2}{\Delta x_1(\Delta x_1 + \Delta x_2)}$$

$$\Delta x_1 = x_j - x_{j-1}$$

$$\Delta x_2 = x_{j+1} - x_j$$

For locally supersonic flow a first-order backward difference formula is used and is given by

$$\lambda\phi_{XX} = \left[\beta^2 - M_\infty{}^2(\gamma+1)C(\phi_{j,k} - \phi_{j-2,k})\right]\left[D1\phi_{j,k} + D2\phi_{j-1,k} + D3\phi_{j-2,k}\right] \tag{13}$$

where

$$C = \frac{1}{\Delta x_1 + \Delta x_2}$$

$$D1 = \frac{2}{\Delta x_2(\Delta x_1 + \Delta x_2)}$$

$$D2 = \frac{-2}{\Delta x_1 \Delta x_2}$$

$$D3 = \frac{2}{\Delta x_1(\Delta x_1 + \Delta x_2)}$$

$$\Delta x_1 = x_{j-1} - x_{j-2}$$

$$\Delta x_2 = x_j - x_{j-1}$$

In the case of a supersonic free stream an evenly spaced x-grid is placed over the entire flow field, and either equation (10) or (11) is used for $\lambda\phi_{XX}$ at every point.

In the radial direction the finite difference grid spacing is given by the coordinate transformation

$$\eta = \frac{br}{ar + 1} \tag{14}$$

having the inverse transformation

$$r = \frac{\eta}{b - a\eta} \tag{15}$$

With the η-grid equally spaced and with appropriate choices of the parameters a and b, the grid spacing in r will be fine near the body where the radial gradients are large and relatively much coarser at large distances from the body where the gradients are small. Note that an equally spaced grid in r is obtained by setting a = 0 and b = 1.

The finite-difference approximation to the radial derivative in equation (1) is given in terms of η by the second-order central difference formula

$$\left[\frac{1}{r}(r\phi_r)_r\right]_{j,k} = A_k\phi_{j,k-1} - B_k\phi_{j,k} + C_k\phi_{j,k+1} \tag{16}$$

where

$$A_k = \frac{(b - a\eta_k)^3}{b(\Delta\eta)^2}\left[\frac{b - a\eta_k}{b} - \frac{\Delta\eta}{2}\left(\frac{1}{\eta_k} - \frac{2a}{b}\right)\right]$$

$$B_k = \frac{2(b - a\eta_k)^4}{b^2(\Delta\eta)^2}$$

$$C_k = \frac{(b - a\eta_k)^3}{b(\Delta\eta)^2}\left[\frac{b - a\eta_k}{b} + \frac{\Delta\eta}{2}\left(\frac{1}{\eta_k} - \frac{2a}{b}\right)\right]$$

Boundary Conditions

The slender-body boundary condition (eq. (2)) is applied at the r = 0 axis in a manner similar to that of reference 1. The body axis is placed along the lower edge of the first grid cell as shown in figure 3. The finite-difference approximation for the radial derivative at the first radial grid line (k = 1) is expressed in terms of the equally spaced r-grid (a = 0, b = 1) as

$$\left[\frac{1}{r}(r\phi_r)_r\right]_{j,1} = \frac{(r\phi_r)_{j,3/2} - (r\phi_r)_{j,1/2}}{r_1\Delta r}$$

$$= \frac{r_{3/2}\dfrac{(\phi_{j,2} - \phi_{j,1})}{\Delta r} - R\dfrac{dR}{dx}}{r_1\Delta r} \tag{17}$$

In terms of the transformed variable η this approximation becomes

$$\left[\frac{1}{r}(r\phi_r)_r\right]_{j,1} = -B_1\phi_{j,1} + C_1\phi_{j,2} + A_1\left(R\frac{dR}{dx}\right) \tag{18}$$

where

$$B_1 = C_1 = \frac{(2b - a\Delta\eta)^3(b - a\Delta\eta)}{4b^2(\Delta\eta)^2}$$

$$A_1 = -\frac{(2b - a\Delta\eta)^3}{4b^2(\Delta\eta)^2}$$

Since the derivative is expressed in terms of $r\phi_r$ this formula avoids the singularity at the axis, and together with equation (16) leads to a tridiagonal matrix for the coefficients of ϕ along each radial line.

The values of ϕ at the body surface needed to compute the surface pressure coefficients were obtained by second-order interpolation formulas when the body surface was between k = 1 and k = 2, as shown in figure 3. When the body surface was between k = 1 and the body axis, the $ln(r)$ variation of ϕ assumed by first-order slender-body theory was taken into account and the quantity $\phi/ln(r)$ was extrapolated to the body surface. Numerical studies showed that the best results were obtained when the k = 1 grid line was everywhere inside or on the body surface, thus avoiding the extrapolation but requiring that Δr be very small near the axis.

The treatment of the far field boundaries for a slender body in free air depends on whether the free stream is subsonic or supersonic. In the case of a subsonic free stream the approach in this report was to use coordinate stretching to place the free-stream boundary at infinity in the radial direction, and at least two body lengths[1] fore and aft of the body in the free-stream direction. This approach is applicable to sonic as well as subsonic free-stream velocities, an advantage over using an integral equation as in reference 1.

In the case of a supersonic free stream the lack of upstream influence in the far field allows the boundaries to be placed closer to the body. The computational domain must be sufficiently large, however, to include any embedded subsonic regions behind the detached bow shock or the rear recompression shock. The radial boundary must also be sufficiently far removed so that disturbances reflected from the boundary do not impinge on the body surface.

The open jet and porous wall boundary conditions were applied at a fixed radial distance corresponding to the average cross-sectional area of the actual wind-tunnel test section. The open jet boundary condition (eq. (3)) corresponds to a constant perturbation potential, which for convenience is set to zero in the numerical calculation.

[1] This condition was established by numerical experiments.

The porous wall boundary condition given by equation (4) is satisfied by approximating the derivative ϕ_r at k = km with a three-point backward difference formula. When the flow at the wall is subsonic, ϕ_x is replaced by a two-point central difference to give

$$\phi_{j,km} = \frac{1}{3}\left[4\phi_{j,km-1} - \phi_{j,km-2} - \frac{P}{H\,\Delta x}\,(\phi_{j+1,km} - \phi_{j-1,km})\right] \tag{19a}$$

where

$$H = \frac{(b - a\eta_{km})^2}{b\,\Delta\eta}$$

When the flow is supersonic, ϕ_x is replaced by a three-point backward difference to give

$$\phi_{j,km} = \frac{1}{3(H\,\Delta x + P)}\left[H\,\Delta x(4\phi_{j,km-1} - \phi_{j,km-2}) + P(4\phi_{j-1,km} - \phi_{j-2,km})\right] \tag{19b}$$

The wall boundary condition is incorporated into the transonic equation by substituting equations (19) into the radial derivative approximation, equation (16), at k = km − 1. For subsonic flow at the wall equation (16) becomes

$$\left[\frac{1}{r}(r\phi_r)_r\right]_{j,km-1} = \left(A_{km-1} - \frac{C_{km-1}}{3}\right)\phi_{j,km-2} + \left(-B_{km-1} + \frac{4}{3}C_{km-1}\right)\phi_{j,km-2}$$

$$- \frac{PC_{km-1}}{3H\,\Delta x}\,(\phi_{j+1,km} - \phi_{j-1,km}) \tag{20a}$$

and for supersonic flow

$$\left[\frac{1}{r}(r\phi_r)_r\right]_{j,km-1} = \left[A_{km-1} - \frac{H\,\Delta x C_{km-1}}{3(H\,\Delta x + P)}\right]\phi_{j,km-2} + \left[-B_{km-1} + \frac{4H\,\Delta x}{3(H\,\Delta x + P)}\right]\phi_{j,km-1}$$

$$+ \frac{PC_{km-1}}{3(H\,\Delta x + P)}\left[4\phi_{j-1,km} - \phi_{j-2,km}\right] \tag{20b}$$

Relaxation Procedure

The relaxation procedure for solving the transonic problem is illustrated by the finite difference approximations to equation (1) in the case of free air for the equally spaced region shown in figure 2. At interior points

$$-A_k\phi_{j,k-1} + \left[B_k \pm \frac{2\lambda_{j,k}}{(\Delta x)^2}\right]\phi_{j,k} - C_k\phi_{j,k+1} = F_{j,k} \tag{21a}$$

and at points along the body boundary

$$\left[B_1 \pm \frac{2\lambda_{j,1}}{(\Delta x)^2}\right]\phi_{j,1} - C_1\phi_{j,2} = F_{j,1} + A_1 R \frac{dR}{dx} \tag{21b}$$

If the flow is locally subsonic ($\lambda_{j,k} > 0$) the plus sign is used with

$$\lambda_{j,k} = \beta^2 - M_\infty^2(\gamma + 1)\left(\frac{\phi_{j+1,k} - \phi_{j-1,k}}{2\Delta x}\right) \tag{22a}$$

$$F_{j,k} = \frac{\lambda_{j,k}}{(\Delta x)^2}\left[\phi_{j+1,k} + \phi_{j-1,k}\right] \tag{22b}$$

If the flow is locally supersonic ($\lambda_{j,k} < 0$) the minus sign is used with

$$\lambda_{j,k} = \beta^2 - M_\infty^2(\gamma + 1)\left(\frac{2\phi_{j,k} - \phi_{j-1,k} - 2\phi_{j-2,k} + \phi_{j-3,k}}{2\Delta x}\right) \tag{23a}$$

$$F_{j,k} = \frac{\lambda_{j,k}}{(\Delta x)^2}\left[-5\phi_{j-1,k} + 4\phi_{j-2,k} - \phi_{j-3,k}\right] \tag{23b}$$

In the course of the relaxation, the right side of equations (21) is always computed first. The procedure used was to evaluate $\lambda_{j,k}$ using equation (22a) at each point along a grid column (j = const). For $\lambda_{j,k}$ positive, $F_{j,k}$ is calculated by means of equation (22b) and the calculation proceeds to the next point along the column. If $\lambda_{j,k}$ is negative, it is recalculated from equation (23a) and $F_{j,k}$ is found from equation (23b). If $\lambda_{j,k}$ is negative from equation (22a) but positive from equation (23a), $\lambda_{j,k}$ and $F_{j,k}$ are set equal to zero (corresponding to locally sonic flow).

Once the right side of equations (21) is calculated for one column, the entire column can be advanced one iteration. If the advanced results are used to replace the previous ones before the adjacent column is advanced, the method is referred to as successive line overrelaxation (SLOR). This is the technique used in all the computations reported here.

The details may be described as follows. First define the km − 1 dimensional column vector whose elements are the values of the discrete perturbation potential on the *jth* column as

$$\vec{\phi}_j \equiv \begin{pmatrix} \phi_{j,1} \\ \vdots \\ \phi_{j,km-1} \end{pmatrix} \tag{24}$$

Similarly

$$\vec{F}_j = \begin{pmatrix} F_{j,1} \\ \vdots \\ F_{j,km-1} \end{pmatrix} + \text{boundary conditions} \tag{25}$$

Then, equations (21) can be written in the form

$$\underset{\sim}{A}_j \vec{\phi}_j = \vec{F}_j \qquad j = 2, \ldots, jm - 1 \tag{26}$$

which represents $jm - 2$ matrix equations in which each $\underset{\sim}{A}_j$ is a $(km - 1)$ by $(km - 1)$ tridiagonal matrix having elements given by the left side of equations (21). The relaxation technique is then defined by the relation

$$\vec{\phi}_j^{n+1} = \vec{\phi}_j^{n} + \underset{\sim}{\omega}_j \left(\vec{\phi}_j - \vec{\phi}_j^{n} \right) \tag{27}$$

where n is the iteration count, $\vec{\phi}_j$ is the intermediate solution from equation (26), which is solved by a direct algorithm (see ref. 8, p. 195), and $\underset{\sim}{\omega}_j$ is a diagonal matrix of relaxation parameters.

The stability and rate of convergence of the relaxation procedure depend on the choice of relaxation parameters. The present calculations indicate that acceptable choices of relaxation parameters are slightly less than 1 for supersonic regions and between 1 and 2 for subsonic regions (see also refs. 1 and 3). In the transonic problem the matrix generated by the difference equations changes with each iteration. Consequently, it is not possible to determine the optimum relaxation parameter in advance. In the present calculations the rate of convergence was considerably improved by adjusting the relaxation parameters during the relaxation by the use of interactive graphics. In this technique the operator interacts with the computer through a cathode ray tube, which, as the computations proceed, displays the u perturbation velocity field, the residuals, and the iteration count (e.g., see fig. 4). The operator may monitor the solution and adjust the relaxation parameters to achieve rapid convergence and, at the same time, prevent the growth of instabilities.

Before the final results were calculated, studies were conducted to establish an acceptable grid size for the computations. The primary consideration in the choice of streamwise grid size was its effect on shock location and steepness. As a result of these studies, a grid size of $\Delta x = 0.02$ was chosen for the uniform streamwise grid in the vicinity of the body.

A total of 109 streamwise grid points was used for the $M_\infty \leqslant 1$ cases. The equally spaced middle region (refer to fig. 2) was defined by the interval $-0.26 \leqslant x \leqslant 1.26$. The outer, unequally spaced regions were defined by the intervals $-2.36 \leqslant x \leqslant -0.26$ in front of the body and $1.26 \leqslant x \leqslant 3.36$ behind the body. In these regions Δx was successively increased by 20 percent as the boundaries were approached.

In the $M_\infty > 1$ cases an equally spaced streamwise grid was used over the entire flow field. An upstream boundary at $x = -0.2$ was used for all cases while the location of the downstream boundary varied with M_∞, ranging from $x = 1.4$ at $M_\infty = 1.01$ to $x = 1.2$ at $M_\infty = 1.20$.

In the radial direction a 50 point stretched grid was used, except for the free air calculations at $M_\infty = 1$ and 1.01 where 100 points were required to obtain convergence throughout the flow field.

Studies showed that placing the outer radial boundary at infinity in the free air cases is not necessary when the free stream is subsonic. For example, at $M_\infty = 0.99$ the results were insensitive to changes in the boundary location beyond five body lengths, which is about three body lengths above the supersonic region.

DISCUSSION OF RESULTS

The present method has been used to calculate the flow field about a parabolic-arc body of fineness ratio, $f = 10$, with free-stream Mach numbers from $M_\infty = 0.90$ (purely subsonic flow) to $M_\infty = 1.20$ (purely supersonic flow). Converged solutions were obtained in 75 to 300 iterations, the larger numbers corresponding to cases near Mach 1. The computation time varied from 1.5 to 10 minutes on the IBM 360/67 computer.

The pressure coefficients calculated for bodies with and without an aft sting have been compared with measurements presented in reference 9 obtained in the NASA Ames 14-Foot Transonic Wind Tunnel. The wind tunnel has a square ventilated test section consisting of longitudinal slots with corrugated inserts. The data were obtained on an 80-inch model with a turbulent boundary layer at a Reynolds number of approximately 27×10^6. The data were not corrected for wall interference effects. The body was truncated at $x = 0.854$ to permit mounting on the sting.

Subsonic Free Stream

The calculated pressure coefficients for $M_\infty = 0.90$ are shown in figure 5 both on the body and at radial stations from one to four body diameters in the surrounding field. The results computed for the body alone agree well in the region near the forward portion of the body. Much better agreement over the aft portion is obtained when the sting is included in the boundary conditions of the numerical calculations by setting $RdR/dx = 0$ along the sting. Viscous effects, however, are clearly evident near the sting-body juncture.

Results for supercritical flow at free-stream Mach numbers of 0.975 and 0.99 are shown in figures 6 and 7, respectively. The computed values show a slightly more negative C_p as well as a shock location slightly farther downstream than shown by the experimental data. The sting has the effect of moving the embedded shock slightly forward, as expected. The calculated embedded supersonic regions and Mach lines for these two cases are shown in figures 8 and 9. Note, that at $M_\infty = 0.99$ the supersonic region extends approximately two body lengths from the axis. This is almost twice the actual distance to the wind-tunnel wall for the experiments presented in reference 9, and thus wind-tunnel wall interference effects are present.

Sonic Free Stream

The C_p distributions obtained at $M_\infty = 1$ are shown in figure 10. Included in this figure are the theoretical results given by Spreiter and Alksne (ref. 10). The theory of reference 10 assumes that there is a smooth transition from supersonic to subsonic flow along the body surface. The computed results as well as the experimental data, however, show evidence of an embedded shock near the aft portion of the body. The effect of the sting is to cause the computed shock to move upstream, but the predicted location still lies significantly downstream of the experimental shock. The pressure ratio across the computed shock is much less than that required to separate a turbulent boundary layer (given as $p_2/p_1 = 1.89$ in ref. 11, p. 231), and it is reasonable to expect that the disagreement between the predicted and experimental shock location is caused by wind-tunnel wall interference. This question will be discussed later.

Supersonic Free Stream

The computed C_p distributions at $M_\infty = 1.01$ are shown in figure 11. The bow shock appears to be slightly upstream of the experimental location and the computed pressure coefficients are generally less than the experimental values. The addition of the sting strengthens the recompression shock and moves it forward so that it lies just ahead of the sting body juncture but behind the experimental shock. Details of the flow field for $M_\infty = 1.01$ are shown in figure 12. The detached bow wave followed by a large embedded region of subsonic flow is clearly evident. A second embedded subsonic region can be seen at the end of the body.

Computed C_p distributions for supercritical flow with an attached bow shock ($M_\infty = 1.10$) are shown in figure 13. The results agree well with the wind-tunnel measurements. A careful study of the flow field in figure 14 reveals small subsonic regions at the nose and tail.

Finally, figure 15 shows the results for $M_\infty = 1.20$. The entire flow field is supersonic, and the comparisons show good agreement throughout.

Wall Interference Effects

The disagreement between free air inviscid calculations and experimental results can be attributed to both viscous effects and wind-tunnel wall interference. Wind-tunnel wall interference is particularly important very near Mach 1 where the supersonic region in free air may extend well past the walls. In an attempt to minimize the effect of the walls, transonic wind tunnels are often designed with ventilated walls, either slotted or perforated. For the purpose of analysis, a perforated tunnel such as the Ames 14-foot tunnel is treated as one with porous walls. Further, a linearized analysis given in reference 12 suggests that as the free-stream Mach number approaches 1, the blockage effect of porous walls approaches that of an open jet.

Numerical calculations have been made to simulate circular open jet and porous wall wind tunnels having the same cross-sectional area as the Ames 14-foot wind tunnel (tunnel radius = 1.17 body lengths). The C_p distribution on the body surface for various wall porosities and the open jet are compared with the free air calculations and experimental data at $M_\infty = 0.99$ in figure 16. Both the porous wall and open jet calculations show better agreement with experiment just upstream of

the embedded shock. As porosity increases the predicted shock location moves upstream, and the experimental shock lies between that predicted with porosity parameters, $P = 0.5$ and $P = 0.75$. The shock location predicted for the open jet lies significantly upstream of the experimental shock. Since the strength of the computed shocks is not sufficient to cause turbulent boundary-layer separation, the present inviscid calculations give a good prediction for the shock location.

Although the porosity parameter for the Ames 14-foot tunnel has not been directly measured, correlations of unpublished lift interference data at $M_\infty = 0.825$ give an estimate of $P = 0.77$[2] for the Ames 11-foot transonic wind tunnel which has the same wall geometry as the Ames 14-foot tunnel. Thus, this value can be taken as an estimate of the porosity parameter for the 14-foot tunnel and agrees closely with the predicted values.

The results for a porosity parameter of 0.5 and an open jet for $M_\infty = 1.0$ are shown in figure 17 and for $M_\infty = 1.01$ in figure 18. The porous wall calculations agree well with the experimental data over the entire portion of the body from $x = 0$ to 0.8, including the vicinity of the shock. Viscous effects appear in the immediate vicinity of the sting. The open jet calculation again predicts an aft shock location upstream of the measured one. Note that at $M_\infty = 1.01$, the bow shock obtained with the porous wall and open jet boundary conditions lies nearer to the body than that calculated for free air.

Figure 19 presents a comparison of experimental measurements (ref. 9) with numerical calculations for the transonic pressure drag rise. Calculations were carried out for free air conditions and for a porous wind tunnel with a porosity parameter of 0.5. Two groups of experimental points are shown: one obtained by subtracting the experimental base pressure, and theoretical skin friction drag components from the total drag as measured by a force balance, and the other obtained by integrating the measured surface pressures (see ref. 9). The present numerical results include calculations at $M_\infty = 0.80$, 1.025, and 1.05 as well as those Mach numbers previously discussed. It can be seen that the porous wall results agree well with the experimental measurements throughout the drag rise portion of the curve near Mach 1 where wind-tunnel wall interference is expected to be predominant. In contrast, the free air results show a significant departure from the wind-tunnel measurements in this region. In the regions away from Mach 1, the porous wall and free air calculations give nearly the same drag.

CONCLUSIONS

A stable and efficient relaxation method has been described for numerically calculating inviscid transonic flow about slender bodies of revolution. It has been demonstrated that relaxation techniques can be applied throughout the transonic regime, including both subsonic and supersonic free-stream Mach numbers. Good agreement with experimental data on the body surface and in the outer flow illustrates the usefulness of the method in predicting the entire flow field.

[2] Private communication from F. W. Steinle, Ames Research Center, Moffett Field, California, 94035.

Calculations with porous-wall and open-jet boundary conditions have shown the applicability of relaxation techniques to the study of wind-tunnel wall interference. Results for porous walls showed excellent agreement with the wind-tunnel measurements, particularly with regard to the transonic drag rise and the embedded shock location.

Ames Research Center
National Aeronautics and Space Administration
Moffett Field, Calif., 94035, Sept. 21, 1971

REFERENCES

1. Murman, E. M.; and Cole, J. D.: Calculation of Plane Steady Transonic Flows. AIAA J., vol. 9, no. 1, Jan. 1971, pp. 114–121.

2. Murman, E. M.; and Krupp, J. A.: Solution of the Transonic Potential Equations Using a Mixed Finite Difference System. Proc. Second International Conference on Numerical Methods in Fluid Dynamics, Sept. 1970; Lecture Notes in Physics, 1971, pp. 199–206.

3. Steger, Joseph L.; and Lomax, Harvard: Generalized Relaxation Methods Applied to Problems in Transonic Flow. Proc. Second International Conference on Numerical Methods in Fluid Dynamics, Sept. 1970; Lecture Notes in Physics, 1971, pp. 193–197.

4. Ashley, Holt; and Landahl, Marten: Aerodynamics of Wings and Bodies. Addison-Wesley Publishing Co., Reading, Mass., 1965.

5. Glauert, Hermann: Wind-Tunnel Interference on Wings, Bodies, and Airscrews. British A.R.C., R&M 1566, 1933.

6. Goodman, Theodore R.: The Porous Wall Wind Tunnel. Part II – Interference Effect on a Cylindrical Body in a Two-Dimensional Tunnel at Subsonic Speed. Cornell Aeronautical Laboratory, Inc., Rep. AD–594–A–3, 1950.

7. Lax, Peter D.: Weak Solutions of Nonlinear Hyperbolic Equations and Their Numerical Computation. Communications of Pure and Applied Mathematics, vol. 7, no. 1, Feb. 1954, pp. 159–193.

8. Varga, Richard S.: Matrix Iterative Analysis. Prentice-Hall, Inc., Englewood Cliffs, N. J., 1962.

9. Taylor, Robert A.; and McDevitt, John B.: Pressure Distributions at Transonic Speeds for Parabolic-Arc Bodies of Revolution Having Fineness Ratios of 10, 12, and 14. NACA TN 4234, 1958.

10. Spreiter, John R.; and Alksne, Alberta Y.: Slender-Body Theory Based on Approximate Solution of the Transonic Flow Equation. NASA TR R–2, 1959.

11. Chang, Paul K.: Separation of Flow. Pergamon Press, Oxford, 1970.

12. Baldwin, Barrett S.; Turner, John B.; and Knechtel, Earl D.: Wall Interference in Wind Tunnels With Slotted and Porous Boundaries at Subsonic Speeds. NACA TN 3176, 1954.

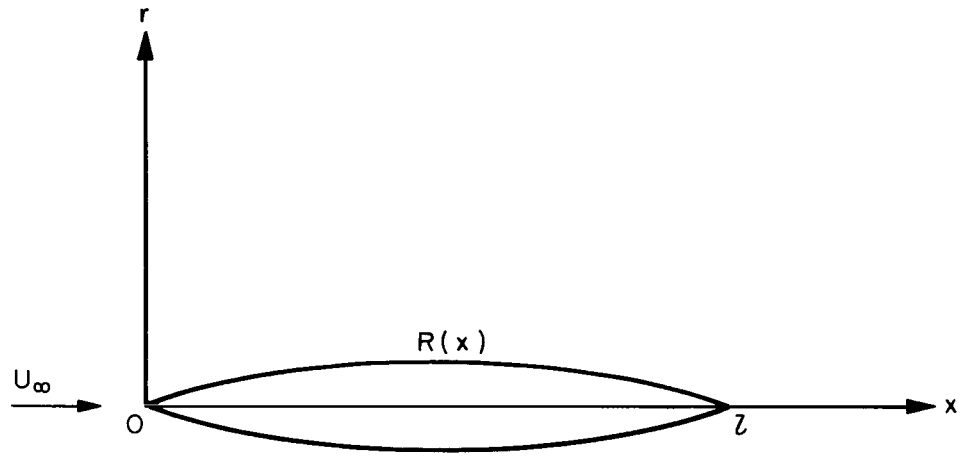

Figure 1.– Body and coordinate system.

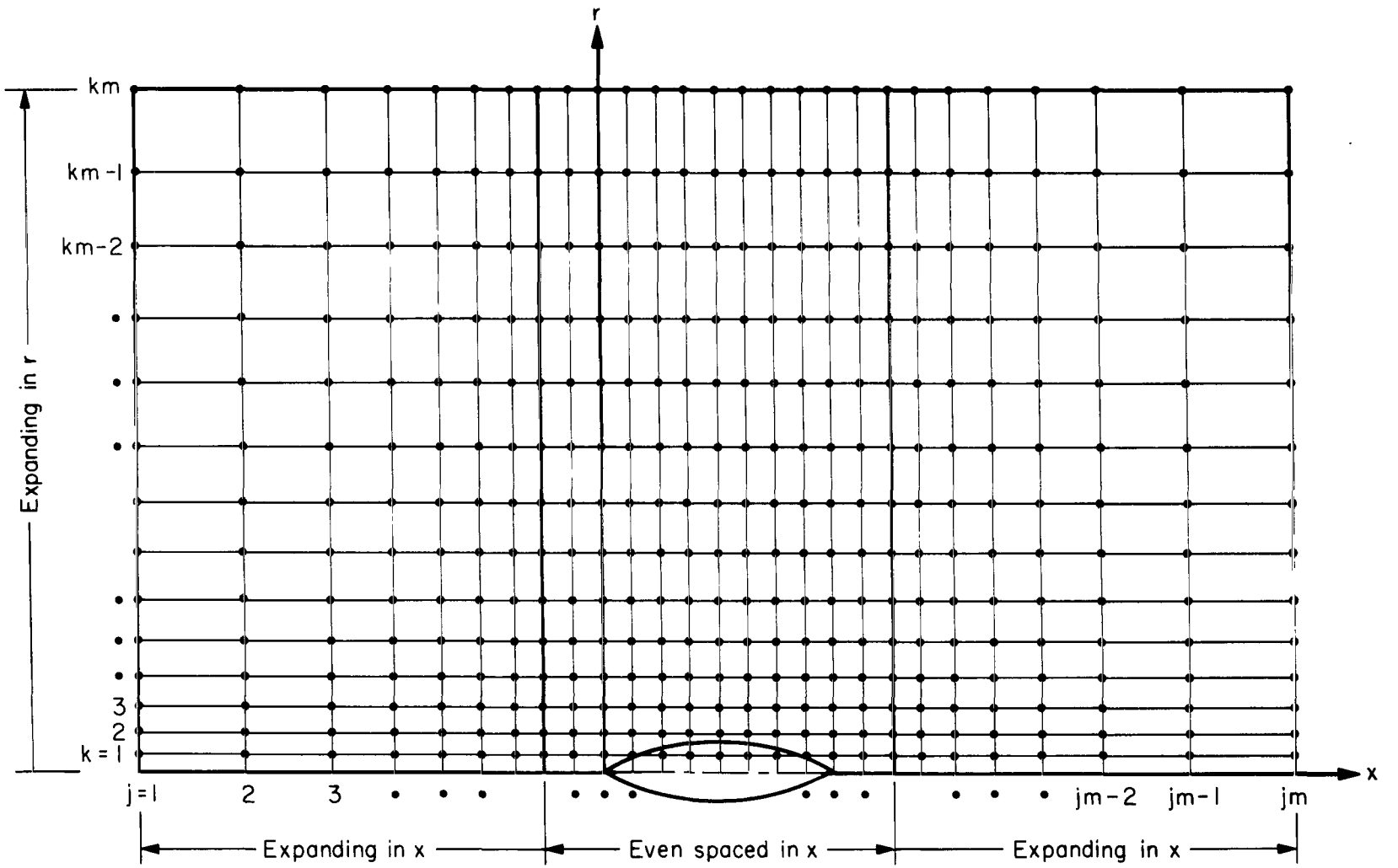

Figure 2.– Finite difference grid.

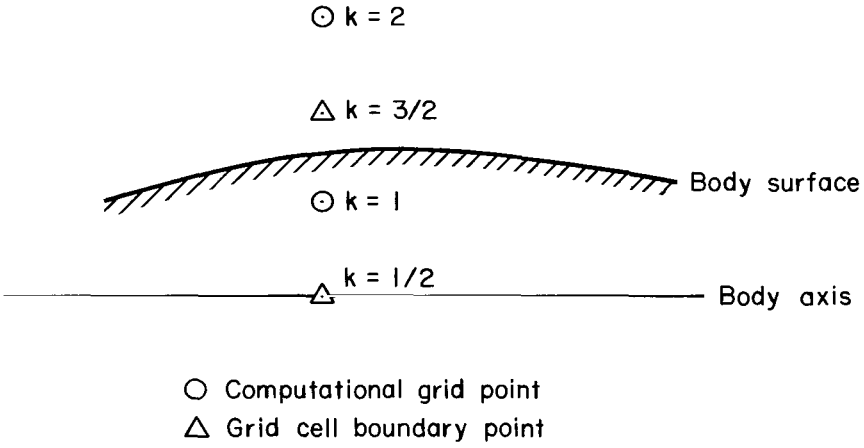

Figure 3.– Radial grid near body.

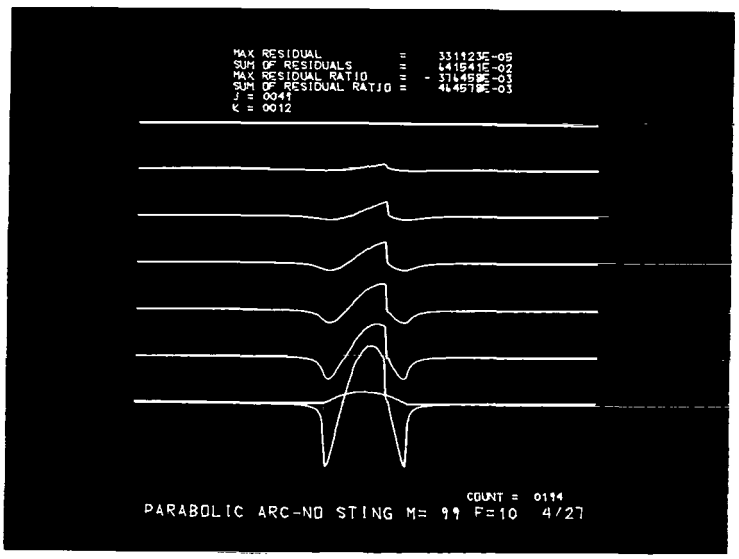

Figure 4.– Interactive graphics display showing u-perturbation velocity.

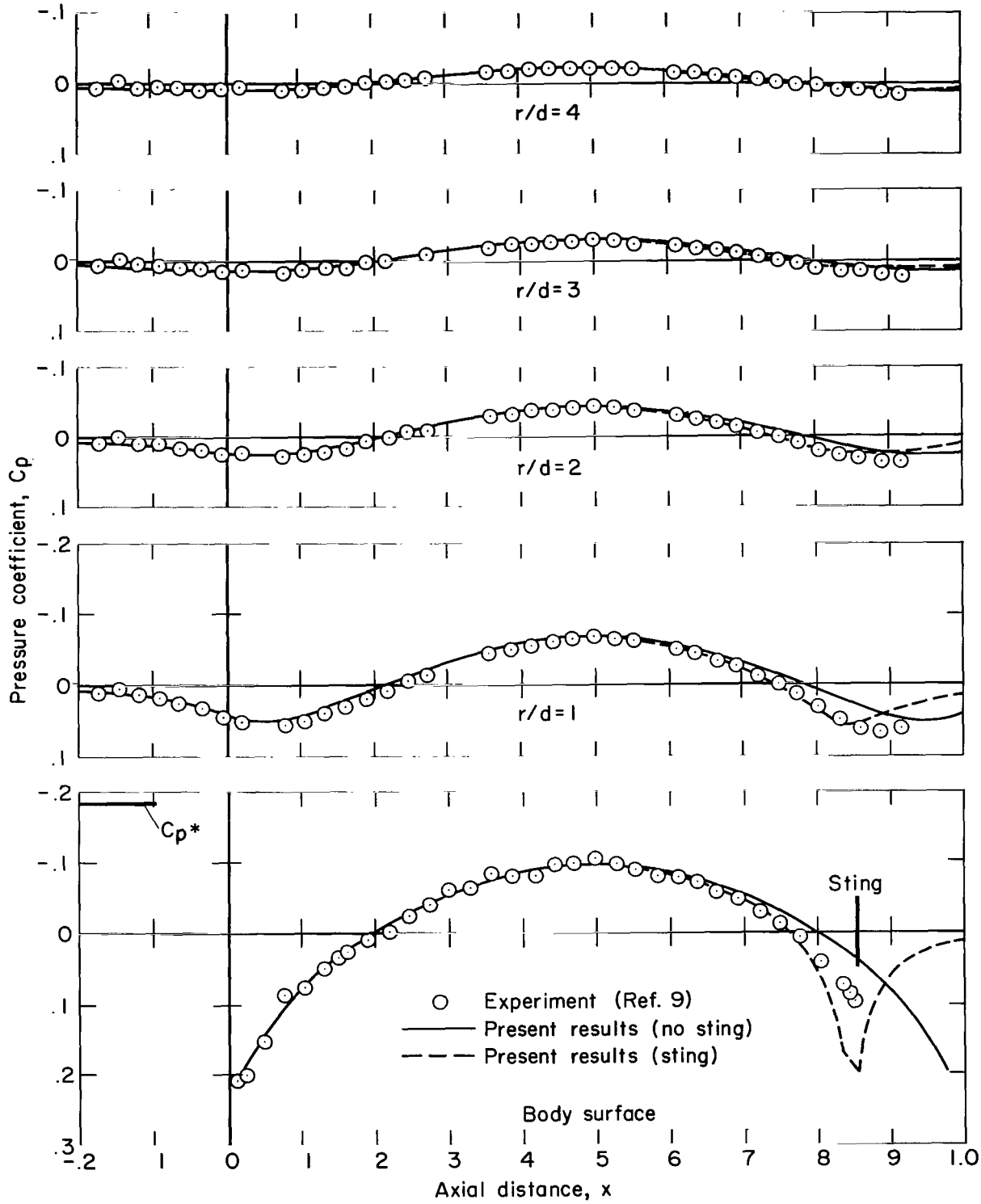

Figure 5.– Distribution of C_p for parabolic arc of revolution ($M_\infty = 0.90$ and $f = 10$).

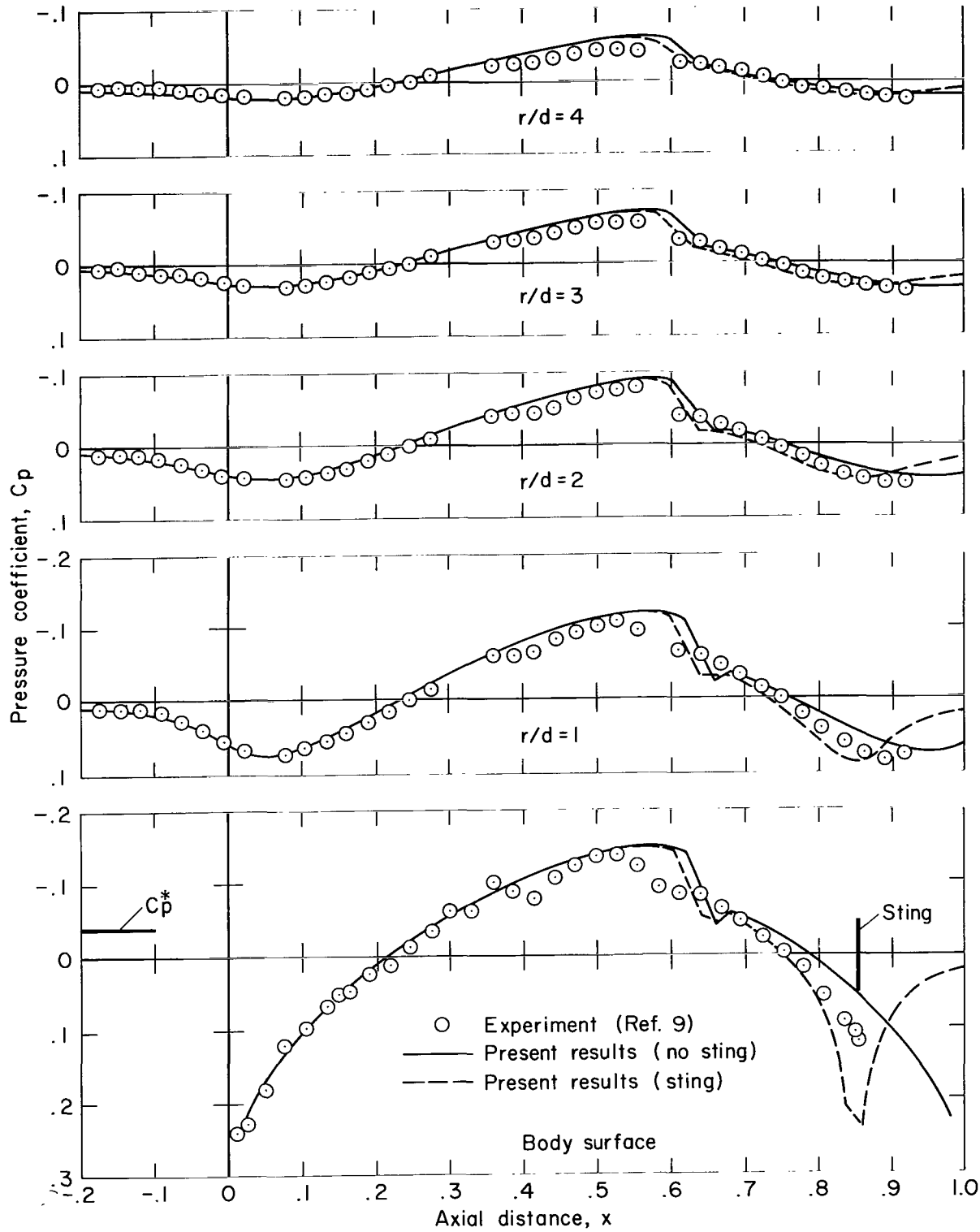

Figure 6.– Distribution of C_p for parabolic arc of revolution ($M_\infty = 0.975$ and $f = 10$).

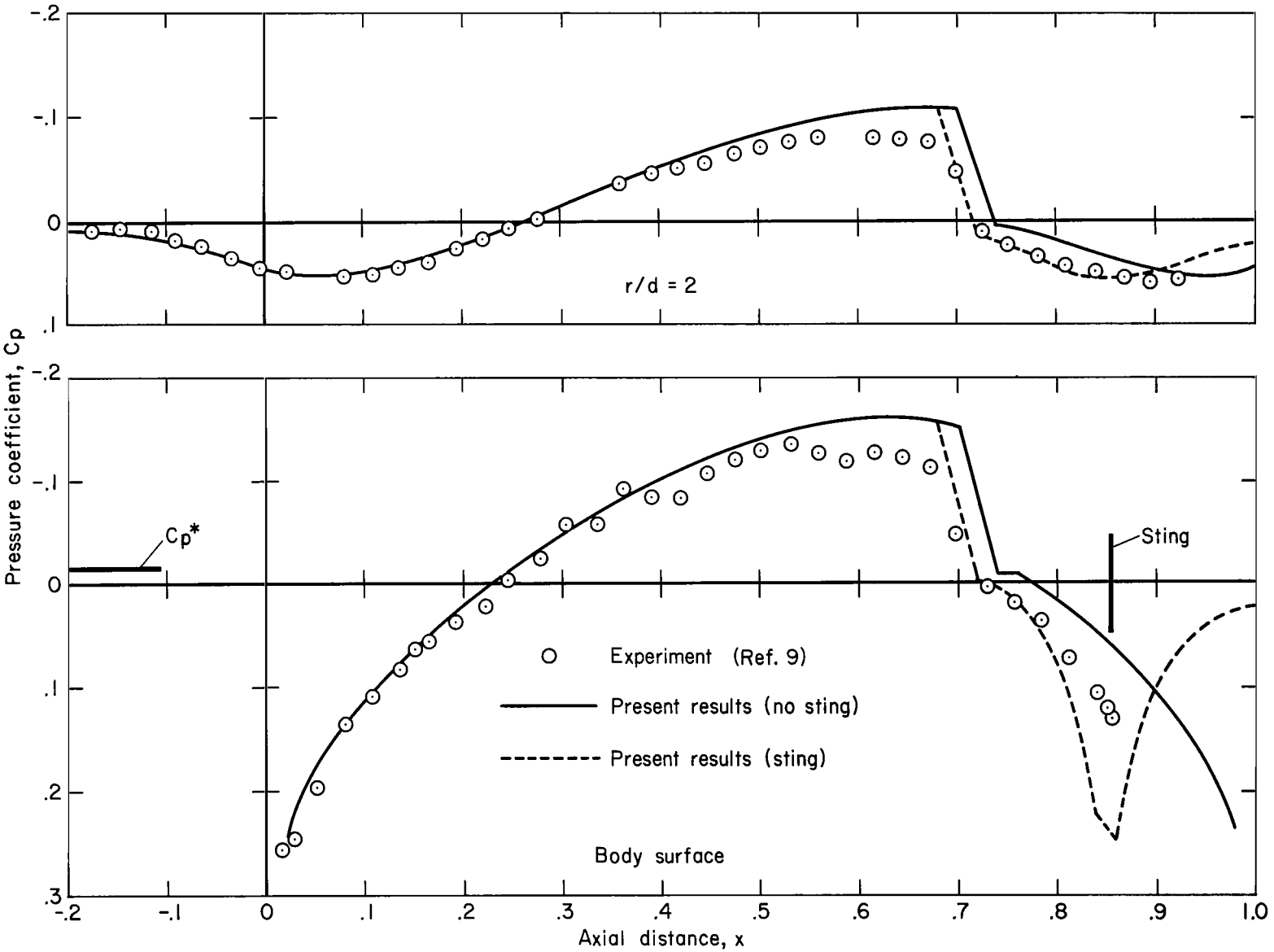

Figure 7.- Distribution of C_p for parabolic arc of revolution ($M_\infty = 0.99$ and f = 10).

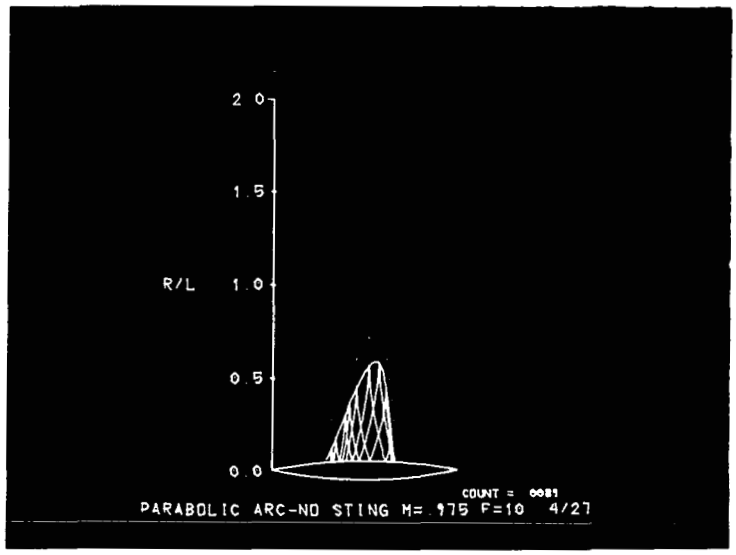

Figure 8.— Supersonic region and Mach lines for a parabolic arc of revolution in free air ($M_\infty = 0.975$ and $f = 10$).

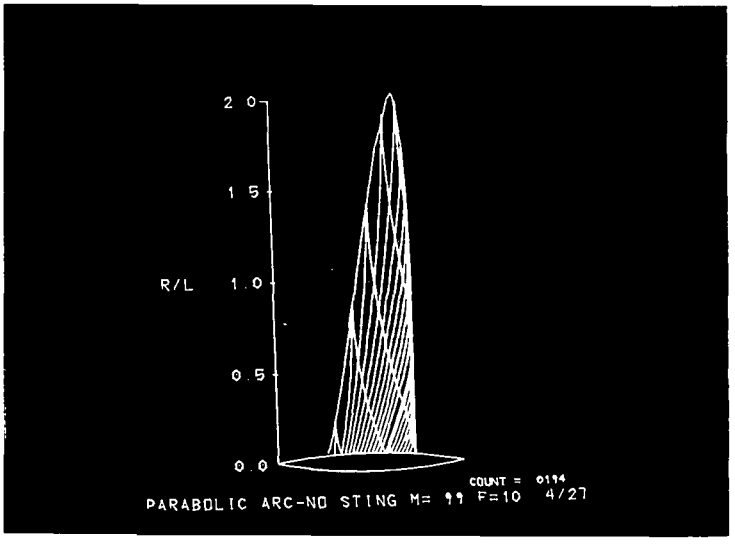

Figure 9.— Supersonic region and Mach lines for a parabolic arc of revolution in free air ($M_\infty = 0.99$ and $f = 10$).

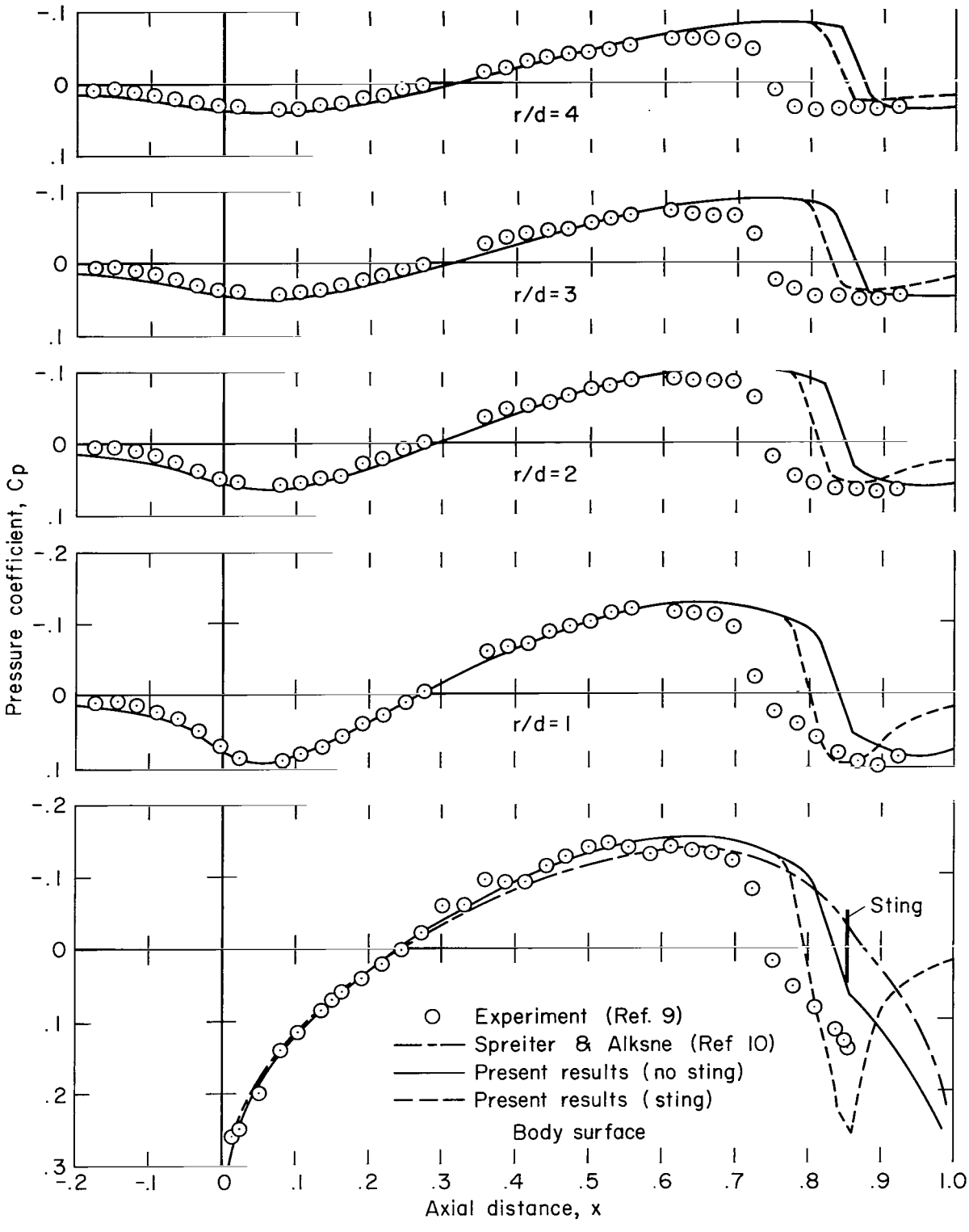

Figure 10.– Distribution of C_p for parabolic arc of revolution ($M_\infty = 1.0$ and $f = 10$).

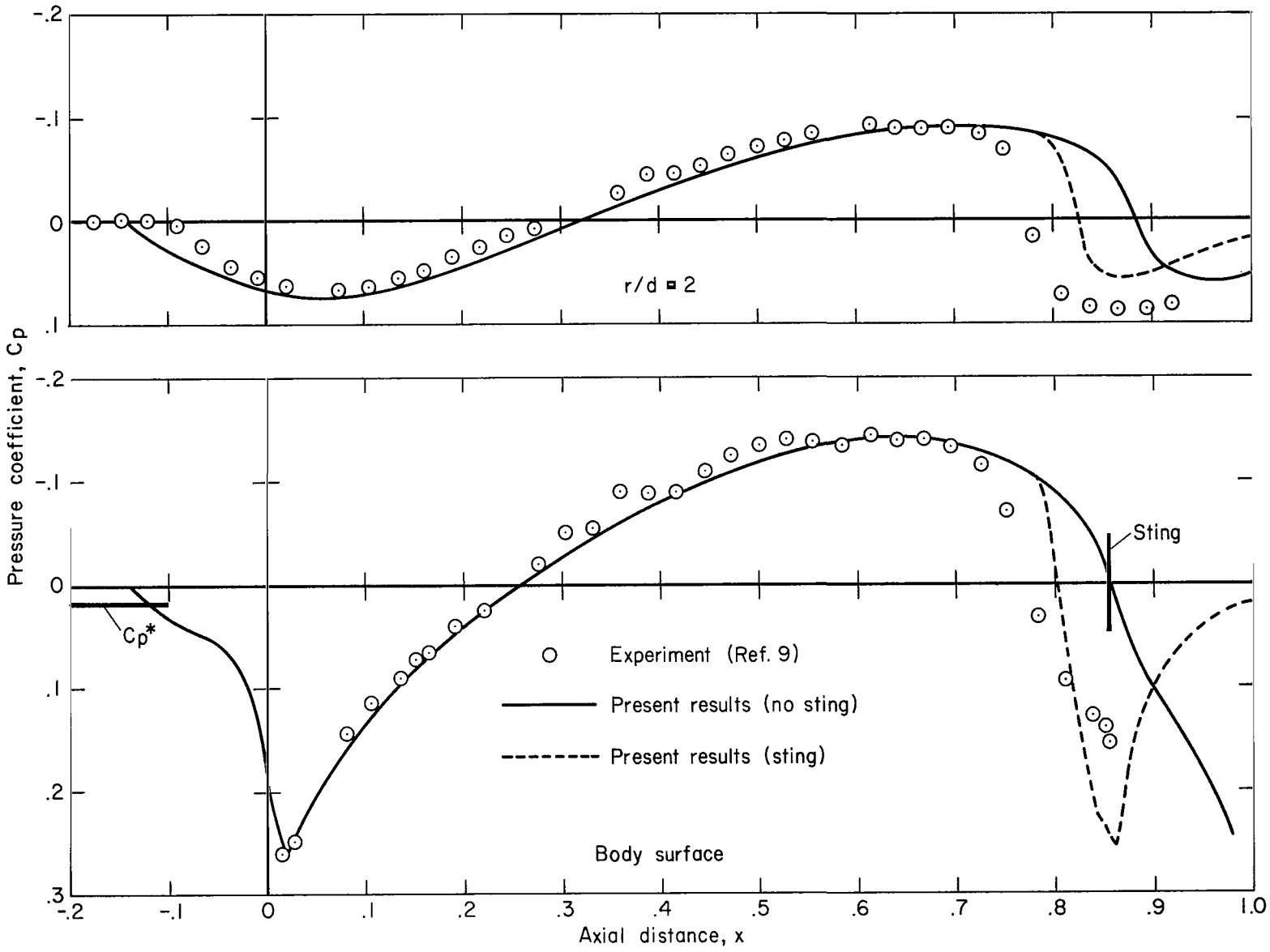

Figure 11.– Distribution of C_p for parabolic arc of revolution ($M_\infty = 1.01$ and $f = 10$).

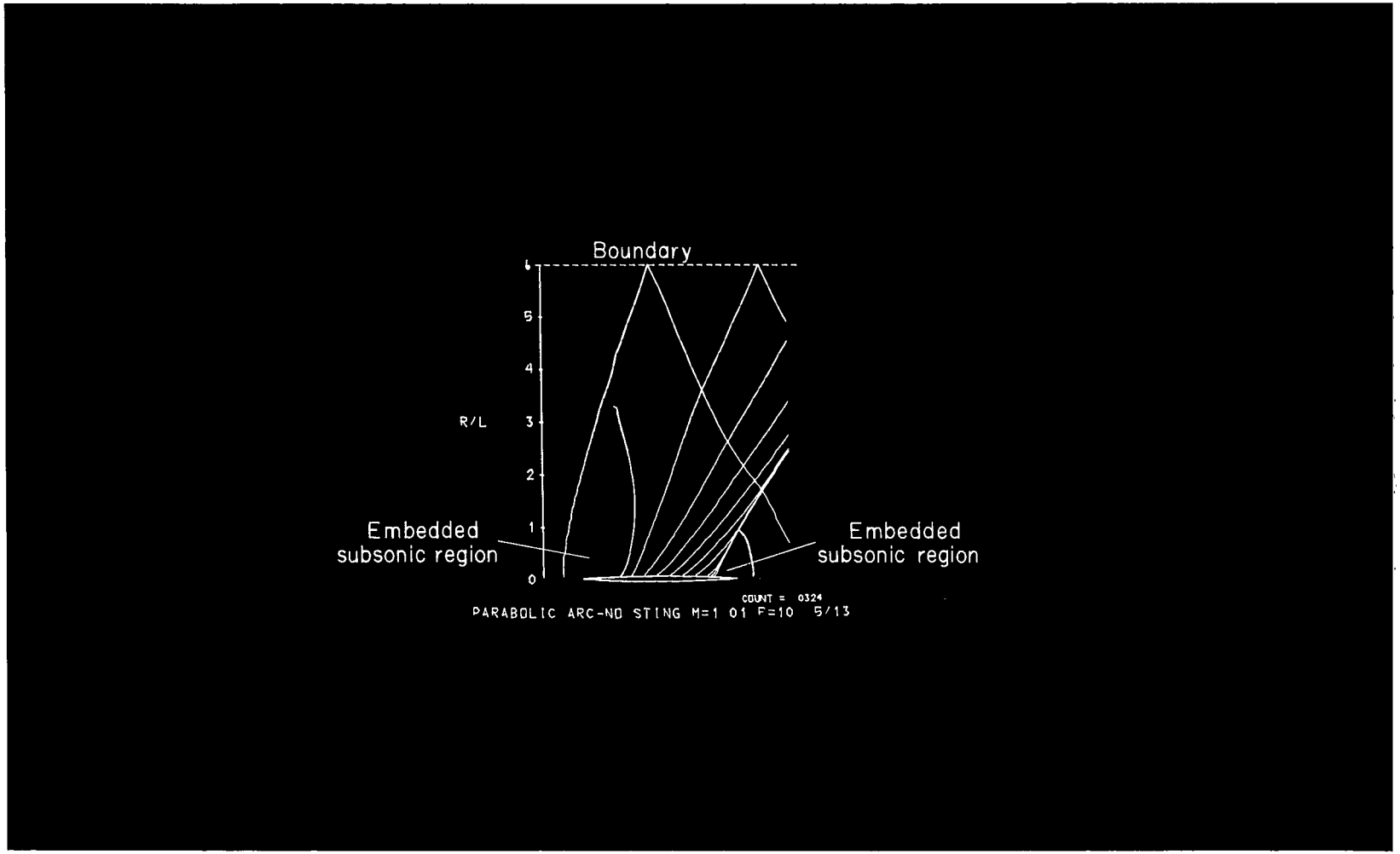

Figure 12.– Transonic flow over parabolic arc of revolution showing bow shock, sonic lines, and Mach lines ($M_\infty = 1.01$ and $f = 10$).

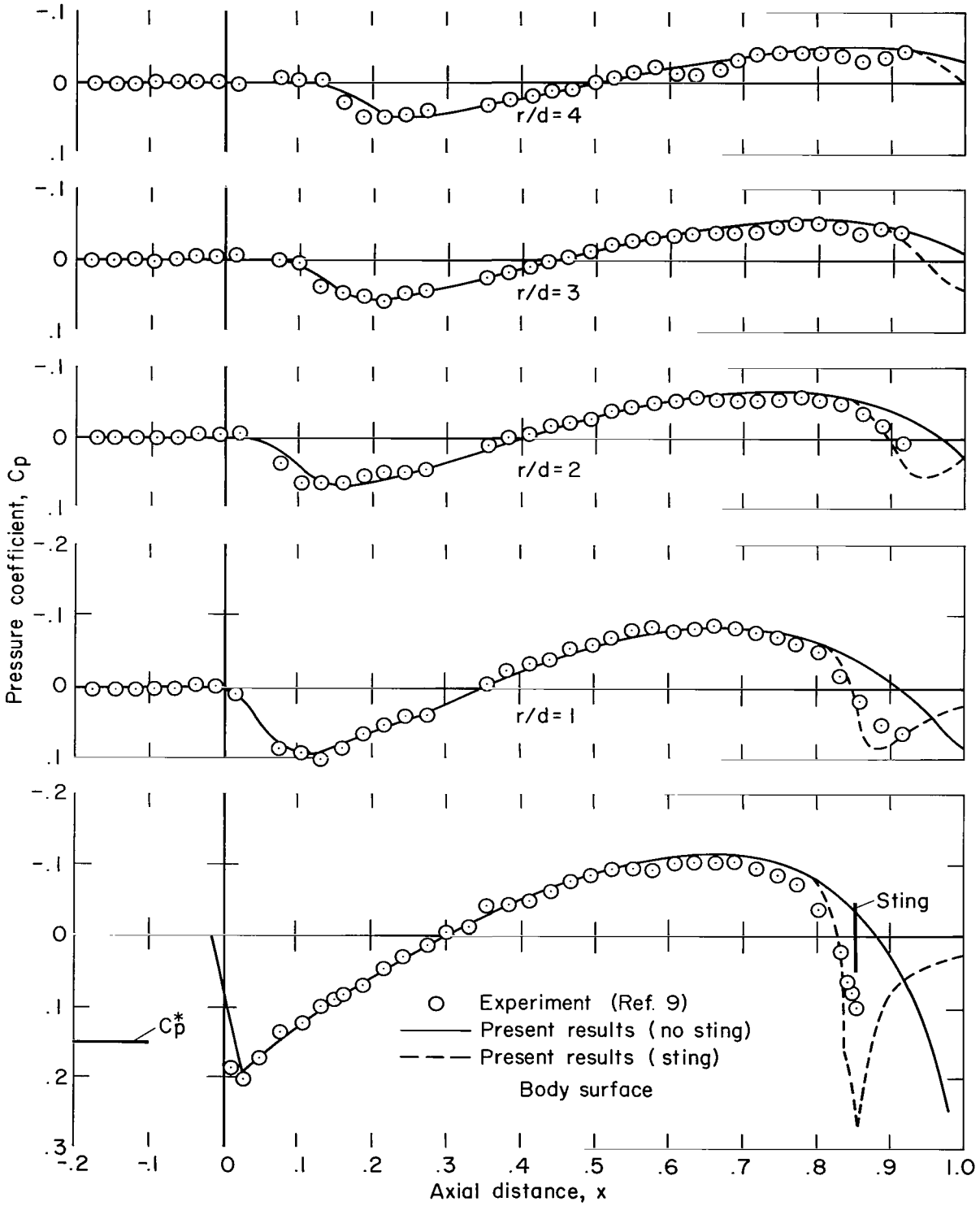

Figure 13.– Distribution of C_p for parabolic arc of revolution ($M_\infty = 1.10$ and $f = 10$).

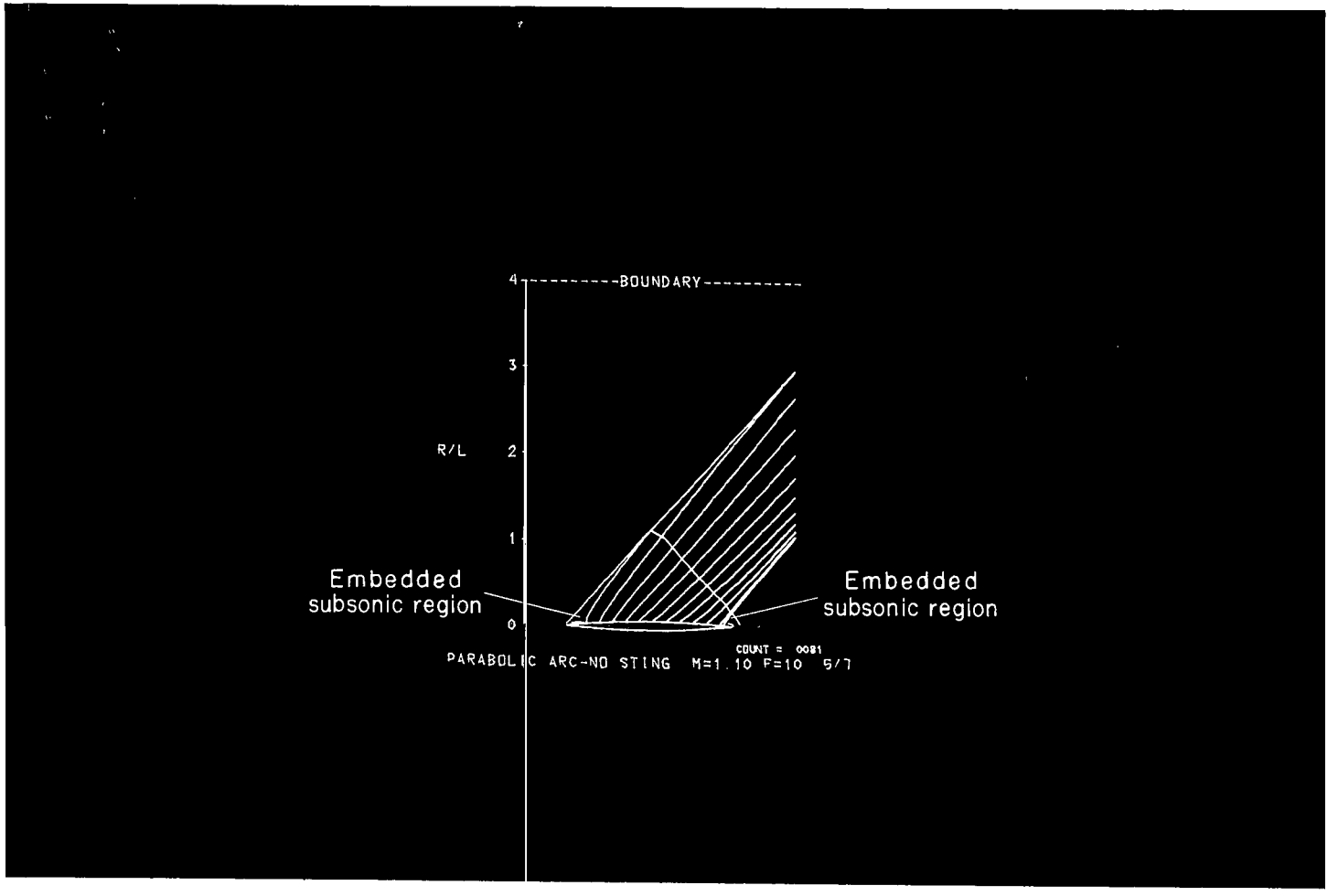

Figure 14.– Transonic flow over parabolic arc of revolution showing bow shock, sonic lines, and Mach lines (M_∞ = 1.10 and f = 10).

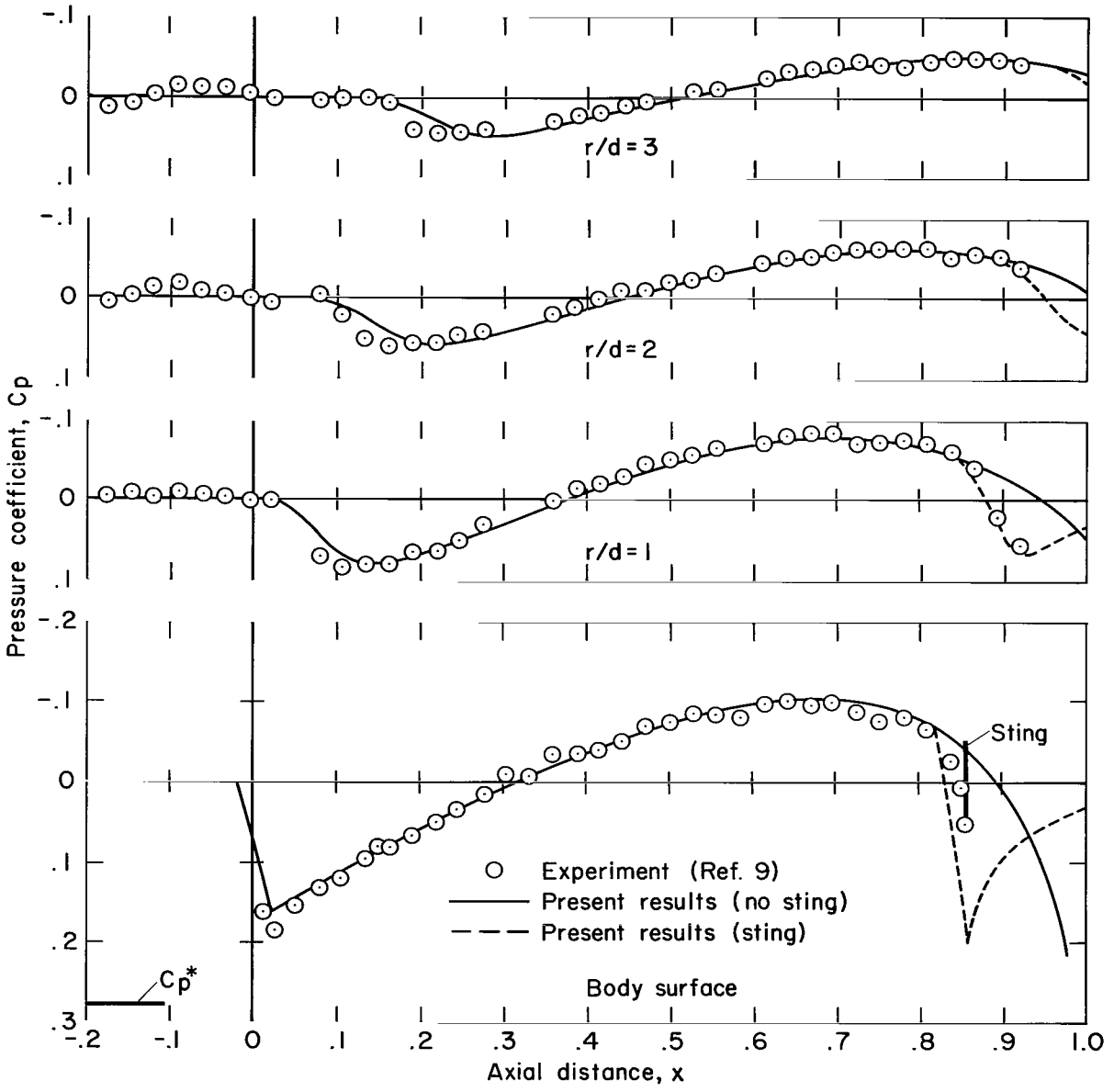

Figure 15.– Distribution of C_p for parabolic arc of revolution ($M_\infty = 1.20$ and $f = 10$).

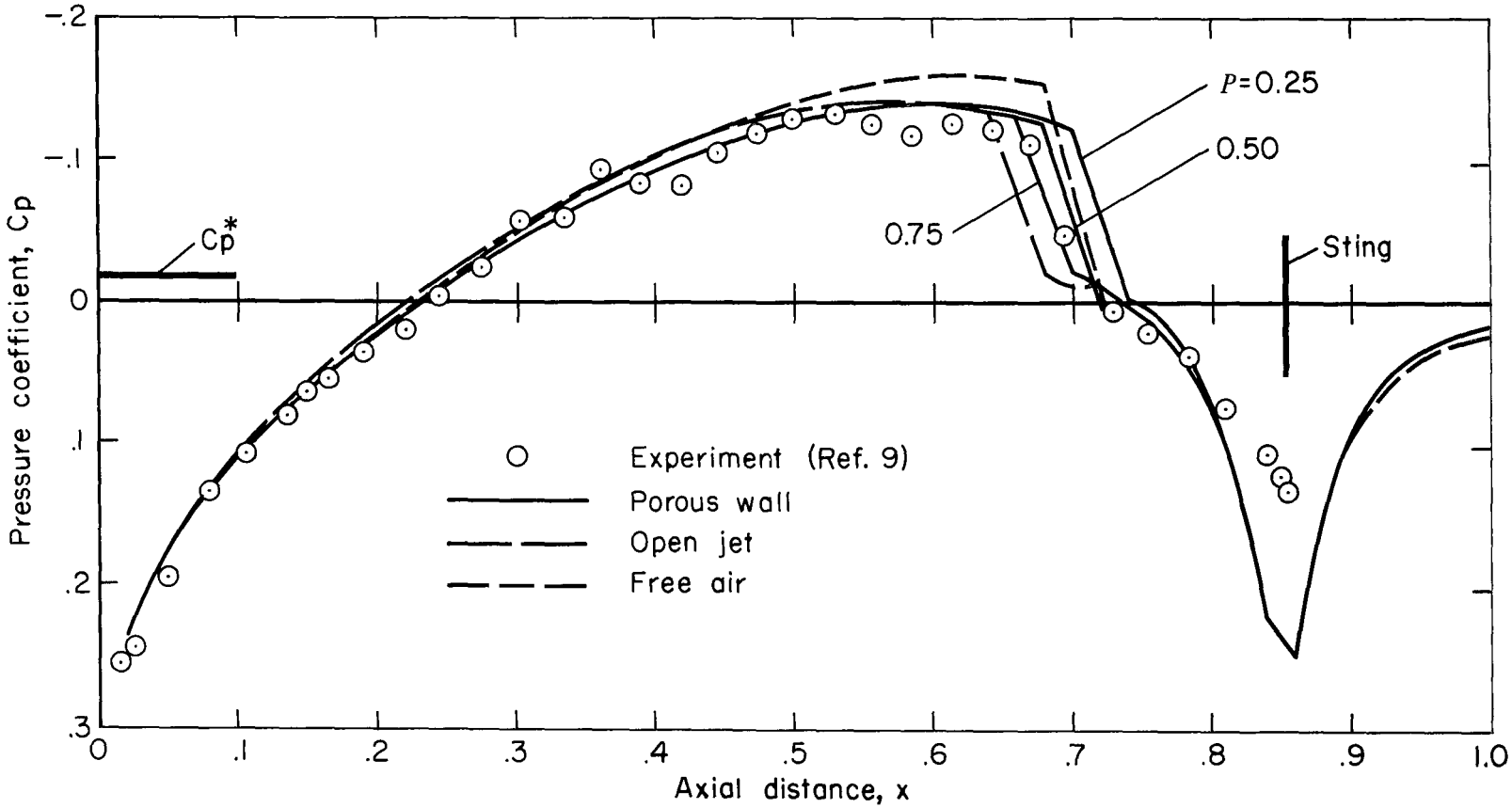

Figure 16.– Effect of wall conditions on body surface C_p for parabolic arc of revolution with sting ($M_\infty = 0.99$ and $f = 10$).

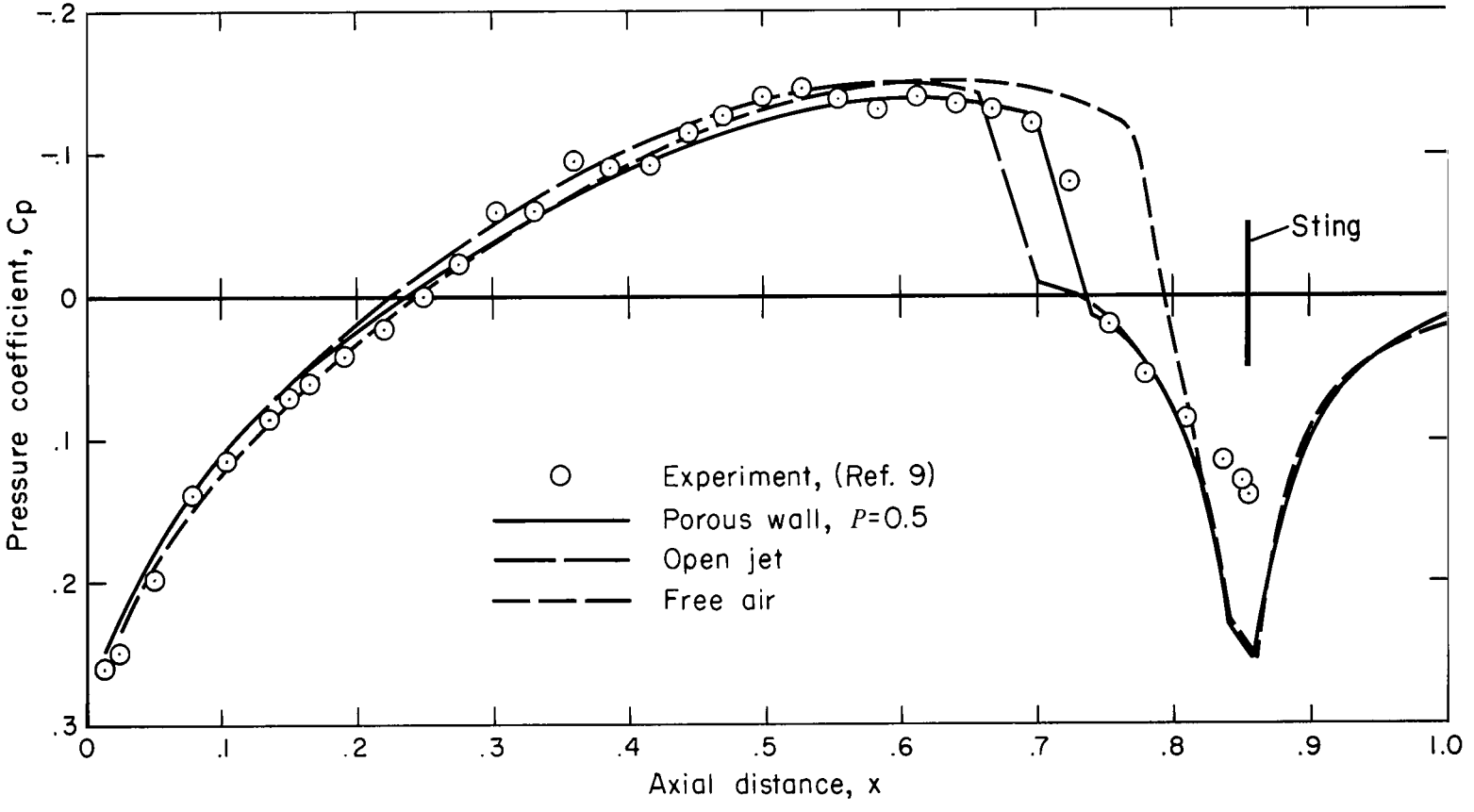

Figure 17.– Effect of wall conditions on body surface C_p for parabolic arc of revolution with sting (M_∞ = 1.0 and f = 10).

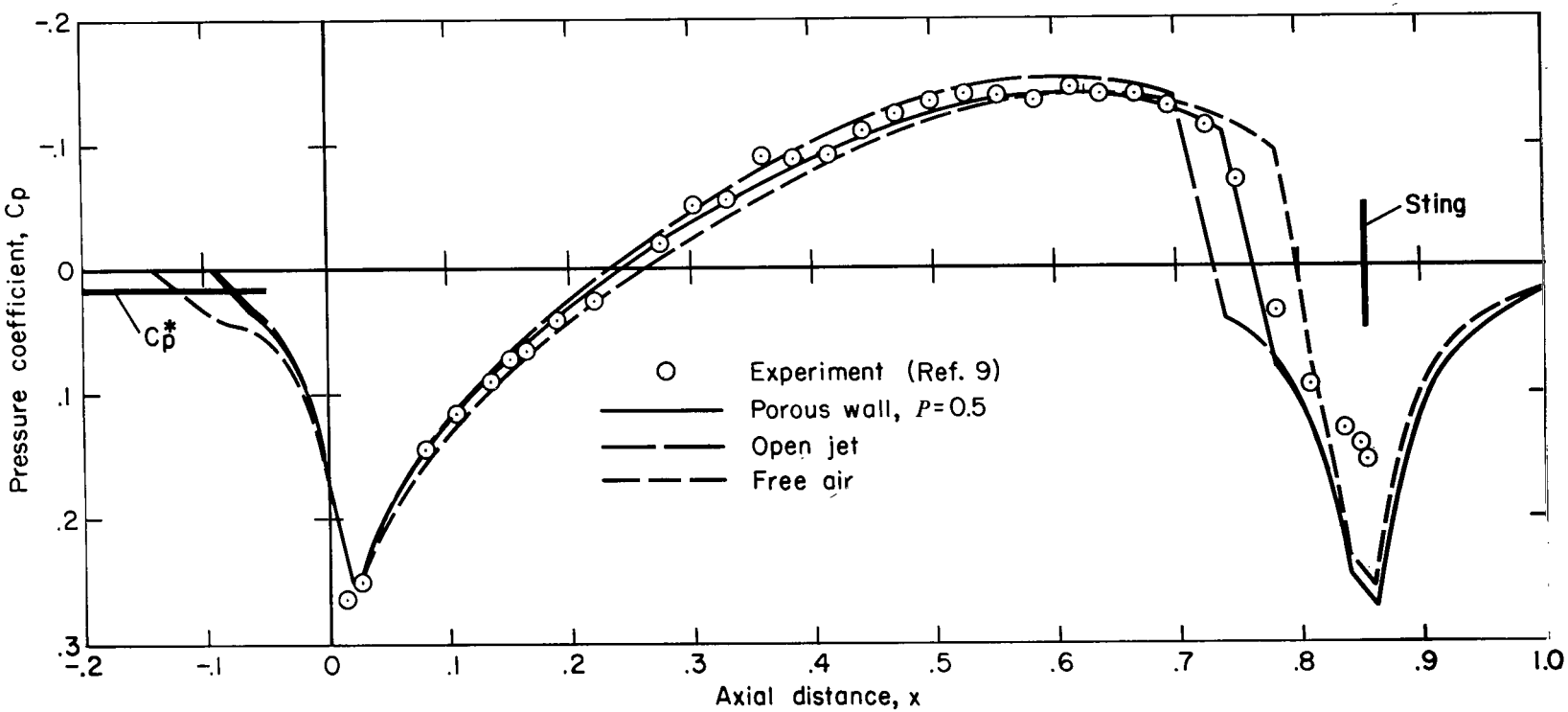

Figure 18.– Effect of wall conditions on body surface C_p for parabolic arc of revolution with sting ($M_\infty = 1.01$ and $f = 10$).

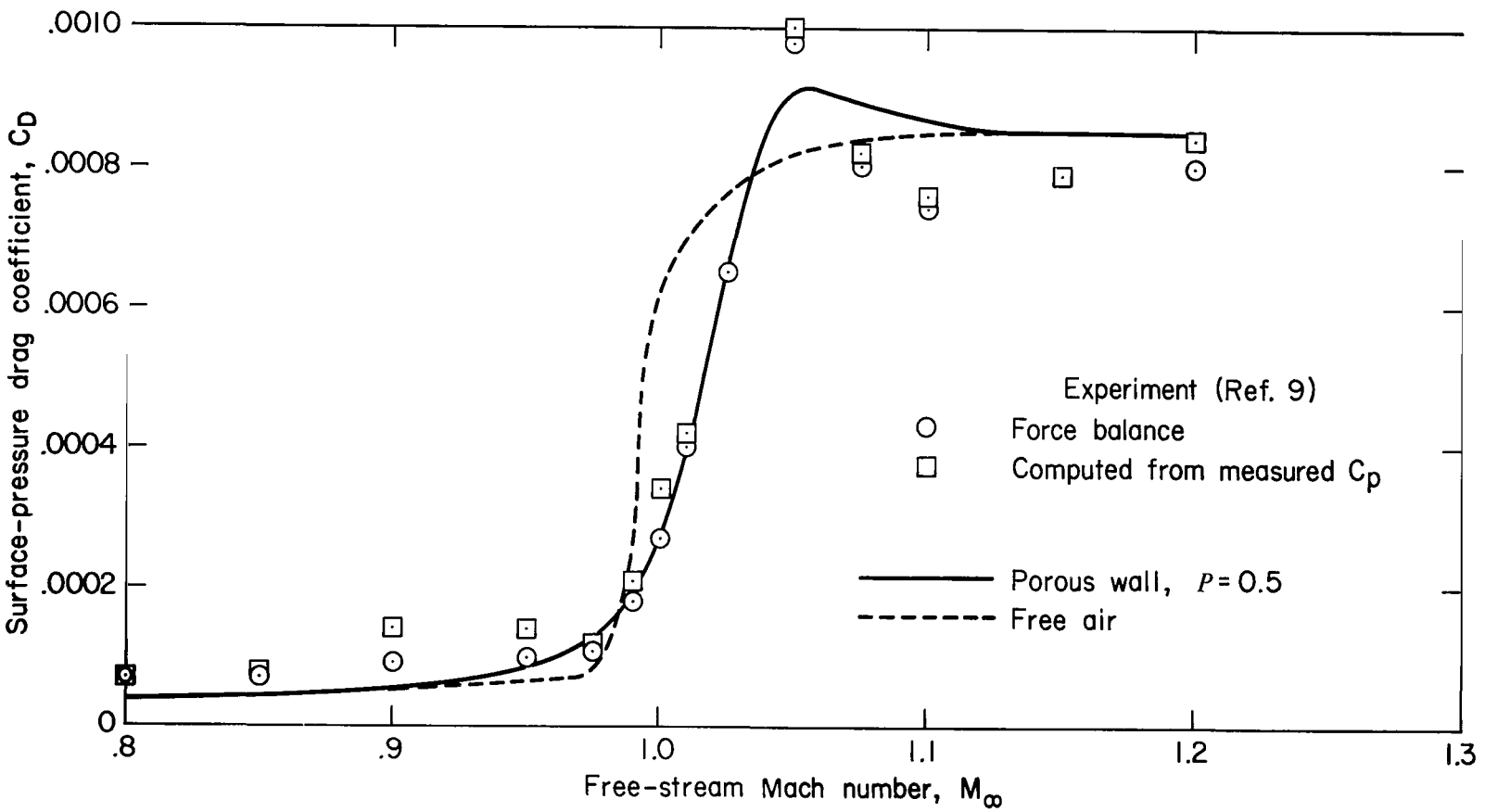

Figure 19.– Variation of surface pressure drag coefficient (based on body length) with Mach number for a parabolic arc of revolution with sting (f = 10).

"The aeronautical and space activities of the United States shall be conducted so as to contribute . . . to the expansion of human knowledge of phenomena in the atmosphere and space. The Administration shall provide for the widest practicable and appropriate dissemination of information concerning its activities and the results thereof."

—NATIONAL AERONAUTICS AND SPACE ACT OF 1958

NASA SCIENTIFIC AND TECHNICAL PUBLICATIONS

TECHNICAL REPORTS: Scientific and technical information considered important, complete, and a lasting contribution to existing knowledge.

TECHNICAL NOTES: Information less broad in scope but nevertheless of importance as a contribution to existing knowledge.

TECHNICAL MEMORANDUMS: Information receiving limited distribution because of preliminary data, security classification, or other reasons.

CONTRACTOR REPORTS: Scientific and technical information generated under a NASA contract or grant and considered an important contribution to existing knowledge.

TECHNICAL TRANSLATIONS: Information published in a foreign language considered to merit NASA distribution in English.

SPECIAL PUBLICATIONS: Information derived from or of value to NASA activities. Publications include conference proceedings, monographs, data compilations, handbooks, sourcebooks, and special bibliographies.

TECHNOLOGY UTILIZATION PUBLICATIONS: Information on technology used by NASA that may be of particular interest in commercial and other non-aerospace applications. Publications include Tech Briefs, Technology Utilization Reports and Technology Surveys.

Details on the availability of these publications may be obtained from:

SCIENTIFIC AND TECHNICAL INFORMATION OFFICE

NATIONAL AERONAUTICS AND SPACE ADMINISTRATION

Washington, D.C. 20546